

A Solar Wind Coronal Origin Study from SOHO/UVCS and ACE/SWICS Joint Analysis

Y.-K. Ko*, T. Zurbuchen[†], L. Strachan*, P. Riley** and J. C. Raymond*

**Harvard-Smithsonian Center for Astrophysics, Cambridge, MA USA*

[†]*Dept of Atmospheric, Oceanic and Space Sciences, University of Michigan, Ann Arbor, MI USA*

***Science Applications International Corporation, San Diego, CA USA*

Abstract. The solar wind ionic charge composition is a powerful tool to distinguish between the slow wind and the coronal-hole associated fast wind. The solar wind heavy ions are believed to be 'frozen-in' within 5 solar radii of the Sun which falls right in the range of SOHO/UVCS coronal observations. We present a joint analysis from SOHO/UVCS and ACE/SWICS which attempts to establish observational evidence of the coronal origin of the solar wind. To connect the solar wind with its coronal origin, we adopt a 3-D MHD model as a guide to link the solar wind at 1 AU to structures in the inner corona. We relate in-situ measured properties of the solar wind (elemental abundances and charge state distributions) with remotely sensed signatures in the corona, namely outflow velocity, electron temperature and elemental abundance.

INTRODUCTION

Solar wind heavy ion composition and elemental abundances are recognized to be a powerful tool to distinguish different types of the solar wind [1]. The solar wind ions measured in-situ are generally 'frozen-in' [2] within 5 solar radii, thus contain the information of the electron temperature (thermal or non-thermal), electron density and ion outflow velocities in the inner corona [3,4]. The mechanisms determining the solar wind elemental abundance are believed to operate at the chromospheric level and the upper transition region [e.g. 5,6]. Therefore the inner corona is the place that is closely related to these solar wind parameters. The UVCS instrument [7] aboard the SOHO spacecraft is designed to observe the solar corona from $1.4 R_{\odot}$ to $10 R_{\odot}$. The spectroscopic data taken by UVCS can be used to derive the ion kinetics, electron temperature, and elemental abundances [8,9]. This provides an ideal opportunity to incorporate both the coronal and the solar wind data to investigate the coronal origin of the solar wind. In this paper, we make such attempts by a joint analysis from SOHO/UVCS and ACE/SWICS. Note that the solar wind plasma measured by ACE should come from near the central meridian. On the other hand, UVCS observes the solar corona above the source region when it rotates to the west limb a few days later. To make comparison between UVCS

and ACE data, we need to assume that the physical properties of the source region/corona do not change significantly within a few days.

UVCS OBSERVATIONS

UVCS observations (for details of the UVCS instrument, see [7]) were made from Oct. 18-24, 1999 at the west limb of the Sun. The observations were composed of two parts. The first part (denoted as 'intensity data') is a mirror scan at 1.5, 1.7, 2.0, 2.5, 3.5, and $4.5 R_{\odot}$ with the objectives of obtaining radial dependences of the coronal plasma properties. The second part (denoted as 'abundance data') is a grating scan at $1.7 R_{\odot}$ with the objectives of obtaining electron temperature and elemental abundances. Every three days (on Oct. 20 and 23) we did a modified plan with the mirror scan at 1.7, 2.0, and $2.5 R_{\odot}$, then we took the same mirror scan but at another grating position. Figure 1 shows the UVCS pointings on Oct. 18, 20, 22, and 24. The slit width was $100 \mu\text{m}$. The field-of-view is thus $28'' \times 40'$.

In October 1999, the Sun was on its way toward solar maximum with the polarity reversal process toward its most active stage (as can be seen from the coronal source surface field maps, <http://quake.stanford.edu/~wso/coronal.html>). The

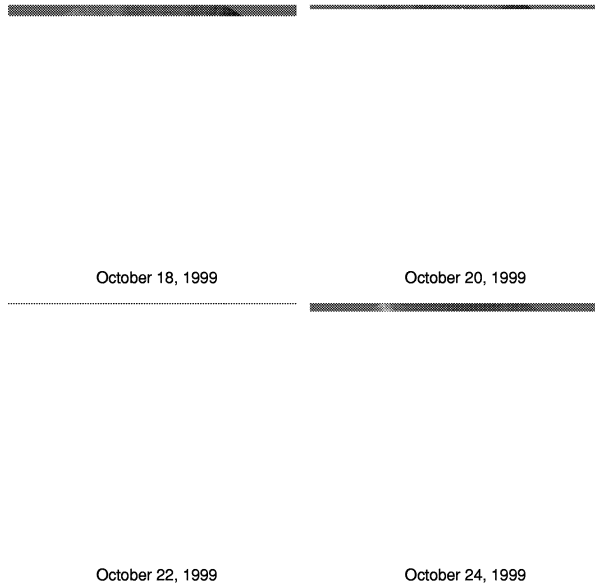


FIGURE 1. UVCS pointings on Oct. 18, 20, 22, and 24 of 1999. Plotted are the OVI channel slit positions on the composite image of EIT 195, UVCS Ly α synoptic (except Oct. 20), and LASCO C2 on those days.

solar magnetic field is far from dipolar. Active regions exist at both low and high latitudes. Equatorial and mid-latitude coronal holes appear replacing the the two polar coronal holes during solar minimum. Correspondingly, the large scale morphology of the corona can change within a day. Around October 5, 1999, a large equatorial coronal hole appeared from the east limb and it was at the west limb when UVCS observation started on Oct. 18. Fig.2 shows the SOHO/EIT 195 image and the NSO/KP He 10830Å coronal hole map on Oct. 13 when this coronal hole was near the disk center. Note that there was a group of active regions at the east side of this coronal hole. Therefore, we can see from Fig.1 that the corona at the west limb during our observation started dark above this coronal hole, then gradually turned bright as those active regions rotated to the limb.

ACE OBSERVATIONS

We use the ion composition and elemental abundance data from ACE/SWICS (for a description of the ACE/SWICS instrument, see [10]) to compare with the coronal plasma properties. Since it takes 2-4 days for the wind plasma of 400-700 km/s to reach ACE, and the source region of the wind will take a few more days to rotate to the west limb,

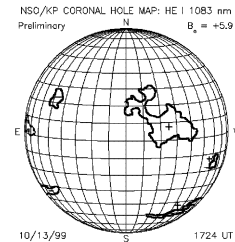


FIGURE 2. SOHO/EIT 195 image at 21:48 UT and the NSO/KP He 10830Å coronal hole map on Oct. 13.

the solar wind plasma would be measured by ACE a few days before its source region would be observed by UVCS. Fig. 3 shows the solar wind He velocity, the O⁺⁷/O⁺⁶ freezing-in temperature, the abundance ratios for (Mg/Mg_{ph})/(O/O_{ph}) (relative to their photospheric values), and (Fe/Fe_{ph})/(O/O_{ph}) from DOY (day-of-year) 286 (Oct. 14) to DOY 296. Note that the abundance for Mg, O, Fe shown here are measured from Mg⁺¹⁰, O⁺⁶, and Fe⁺⁷⁻⁻¹², respectively; therefore they are modulated by the electron temperature where these ions are frozen-in. This is important to realize especially for Mg since Mg⁺¹⁰ ionic fraction increases by 50% if the freezing-in T_e increasing from 6.10 to 6.25 (in log10 scale). We group the data into several time periods according to the solar wind speed and they are represented by different symbols in Fig.3. It is obvious that the fast wind originates from the equatorial coronal hole and it smoothly changes to slow wind in 6 days. Note that since it takes longer for the slow wind to reach ACE, the actual change in wind speed near the Sun should take a much shorter time (see the section below). However, the smooth change from fast to slow wind indicates the crossing of the coronal hole boundary toward the the active regions. It unambiguously implies that this is the period that should relate to the UVCS observations. There was a CME starting around DOY 294 (Oct. 21) which shows features of the magnetic cloud and bi-direction electrons. We thus concentrate on the ACE data before DOY 294.

TRACING THE SOLAR WIND BACK TO THE CORONA

In order to connect the solar wind measured by ACE with its source region, i.e. to know where in longitude and latitude the wind plasma measured at a given time originates from, some kind of trace-back model

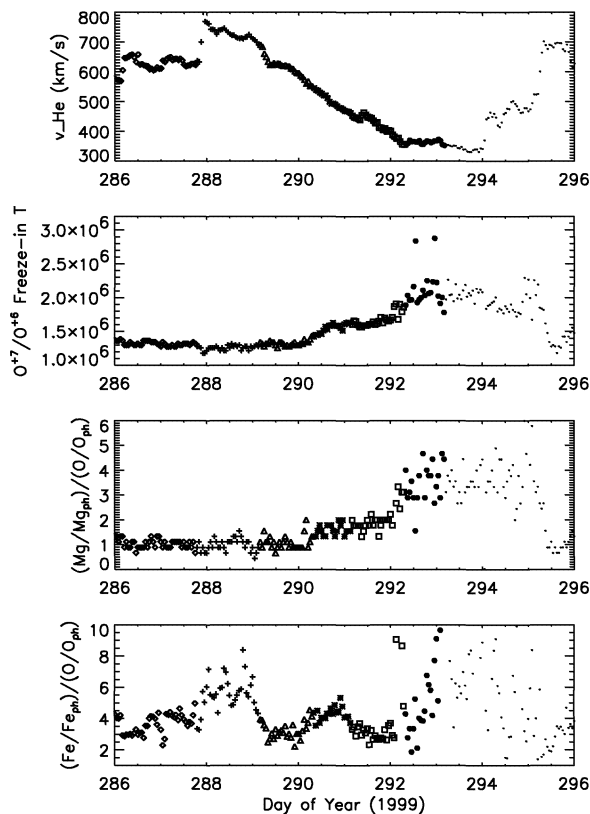


FIGURE 3. He velocity, O^{+7}/O^{+6} freeze-in temperature (in K), Mg/O and Fe/O abundance ratios relative to their photospheric values from ACE/SWICS.

is needed. A common one is the 'ballistic model' (i.e. constant velocity model) which assumes the solar wind trajectory is radial and the speed is constant once it leaves the Sun. Therefore the longitude of the source region mainly depends on the wind speed and the latitude is the same as that of ACE. A more sophisticated approach is to use a 3-D MHD simulation. To facilitate the mapping of ACE solar wind data back to the Sun, we first constructed an equilibrium MHD solution of the solar corona appropriate for the Whole Sun Month observations [e.g. 11,12]. The details of the algorithm used to advance the MHD equations are explained elsewhere [e.g. 13] and here we make a few brief remarks. We restrict ourselves to polytropic solutions and set $\gamma=1.05$ in the corona. This reduced polytropic index provides a very rough approximation of the effects of parallel thermal conduction in the corona. The inner radial boundary condition (at $1 R_{\odot}$) is derived from the observed line-of-sight photospheric magnetic field and the upper radial boundary is set to $30 R_{\odot}$. Reasonable initial values for the magnetofluid parameters are specified and the model is run forward in time

until an equilibrium solution is achieved. We traced field lines from the location of ACE ballistically back to $30 R_{\odot}$, at which point we traced the appropriate field line all the way to the solar surface by this MHD model. The ballistic approximation appears to be a reasonable approximation between $30 R_{\odot}$ and 1 AU where dynamic interactions are only beginning to alter the flow pattern of the solar wind, particularly during solar maximum, and the flow is essentially radial. Within $30 R_{\odot}$, we account for the super-radial expansion of the field lines that can result in a significant shift in the source latitude of the plasma by tracing field lines within the model solution.

Fig.4 plots the source position of the solar wind at 1.0, 1.7, 2.5, 3.5, 4.5 R_{\odot} traced back from the ACE position. For comparison, the ballistic result is also plotted. Note the various symbols indicating respective time period and speed range (cf. Fig.3). One characteristic of the MHD model is that the slow solar wind always originates from the open field region near the coronal hole boundaries and the fast solar wind originates deeper in the coronal hole [11]. The 3-D MHD trace-back results differ from the ballistic one in that the solar wind trajectory is super-radial in the inner corona and the source region can be at different latitude from where ACE is (dotted line. Also compare the latitude of the coronal hole in Fig.2). The MHD model implies that the change-over of the fast wind to the slow wind occurs within 2 days below $2.5 R_{\odot}$, while it is longer in the ballistic model.

CONNECTING THE CORONA AND THE SOLAR WIND

Fig.4 implies that the solar wind source region traced back from the ACE position lies within 15 degrees in latitude north of the equator. The question is if we can see coronal properties that are correlated with those of the solar wind. The task is not easy. The reason is that the observed line intensity is the emissivity integrated along the line of sight. During the early UVCS observations, the coronal hole was very dark and presumably it dominated the line of sight, at least at high heights (cf. Fig.1). Later on, the bright corona (presumably hot and dense materials of the active region loops) gradually rotated into the line of sight. According to the MHD model, the source of the solar wind plasma comes from the region between the coronal hole and the active regions. Some assumptions for the geometry and physical parameters for both structures are needed in order to separate the contributions to the

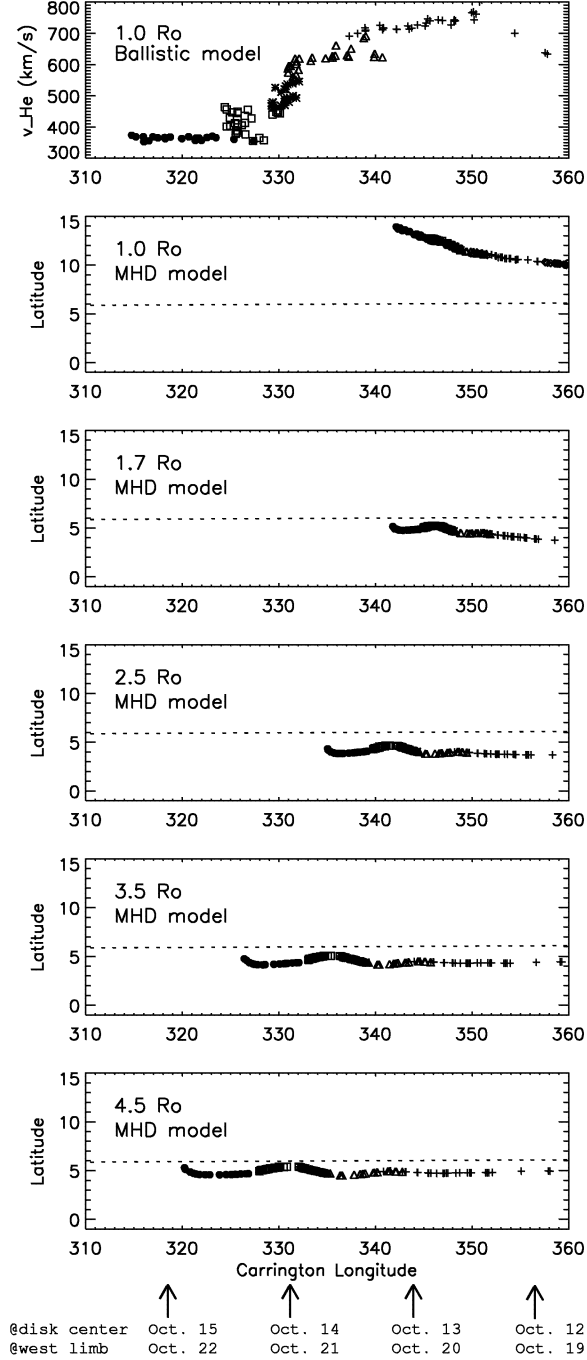


FIGURE 4. The trace-back of the solar wind from the ballistic and 3D MHD models. The approximate dates of the Carrington longitude when it passes the central meridian and the west limb are marked at the bottom of the plots. Different symbols represent different time periods grouped by the solar wind speed (cf. Fig.3). Note that most of the wind data observed by ACE during DOY 286-287 (open diamonds in Fig.3) are mapped back to the previous Carrington rotation, and not shown here.

observed line intensities. For now, we investigate the average coronal properties integrated along the line of sight and compare with the ACE/SWICS data.

For both the intensity and abundance data, we extract two regions: 1) the 'center' region (denoted as 'CT') which is 732 arcsec above the west limb covering 27 to 10 degrees in latitude for 1.5 to 4.5 R_{\odot} , respectively. This is the region that contains the traced-back solar wind from ACE. 2) A 'dark' region (denoted as 'CH') south of the 'CT' region either near the edge of the slit, or, especially at 3.5 and 4.5 R_{\odot} , a dark section which seems to contain more coronal hole material along the line of sight (e.g., see Fig.1, at 4.5 R_{\odot} on Oct. 22). In the following, we will discuss the coronal properties within and between these two regions, and compare them with the solar wind data. Fig. 5 shows the extracted sections for two dates plotted on the Ly α fluxes along the slit.

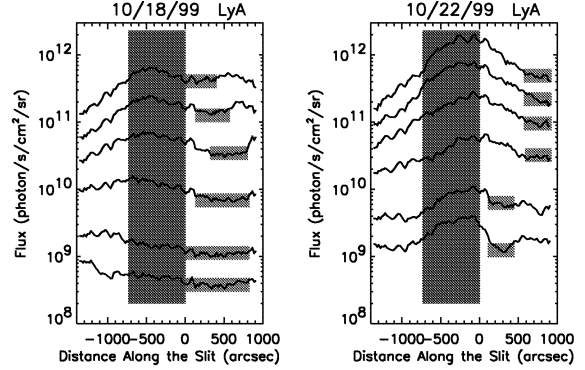


FIGURE 5. Extracted 'CT' (dark shaded areas) and 'CH' (light shaded areas) regions for Oct. 18 and 22. Curves from top to bottom are for 1.5, 1.7, 2.0, 2.5, 3.5, and 4.5 R_{\odot} , respectively. South is toward the right.

Fig.6 plots the Ly α and OVI 1032 kinetic temperatures from the line widths corrected for instrumental broadening, and the OVI 1032 to 1037 intensity ratios versus the observation day at each height. The kinetic temperature is defined from the 1/e width $\delta\lambda$:

$$T_{kin} \equiv \frac{mc^2}{2k} \left(\frac{\delta\lambda}{\lambda} \right)^2 = T_{thermal} + T_{non-thermal}$$

which, without further knowledge of the non-thermal contribution, can be taken as the upper limit of the electron temperature, assuming ions are in thermal equilibrium with the electrons. The OVI 1032/1037 ratio is an indication of the outflow velocity of the O^{+5} ions [e.g. 14] for a given configuration of the electron temperature and density along the line of sight. These parameters are plotted versus time in order to compare with the solar wind data (Fig.3). We can see that: 1) The Ly α T_{kin} increases with time for the first 5 days at every

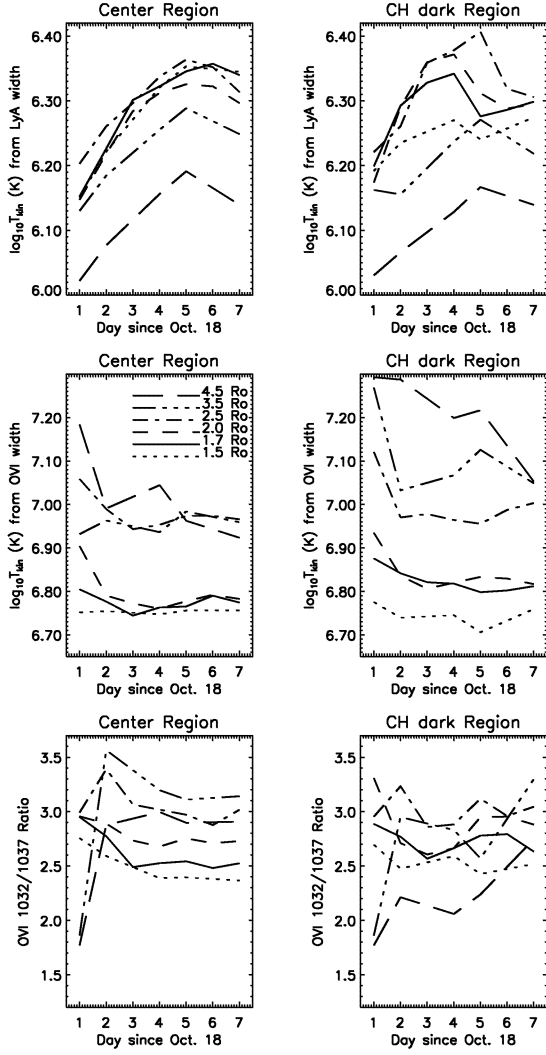


FIGURE 6. Ly α and OVI 1032 kinetic temperatures and the OVI 1032 to 1037 ratio versus time at each height. The line symbols for the heights are indicated on the left-center plot.

height. Those at low heights can be compared with the O^{+7}/O^{+6} freezing-in temperature of the solar wind. For the CT region T_{kin} is approximately the same below $2.5 R_{\odot}$ then decreases at higher heights. 2) The OVI 1032 T_{kin} decreases with time but increases with height. This implies stronger nonthermal heating toward high heights [e.g. 15], especially for the CH region. This dependence of the line widths (i.e. T_{kin}) with height is similar to that of the equatorial streamer [8]. 3) The OVI ratios indicate that substantial outflow starts beyond $3.5 R_{\odot}$. The OVI ratio is expected to increase with height for low outflow speeds ($\ll 100$ km/s) since the density decreases (see Fig.6 below $2.5 R_{\odot}$).

Thus, in general, when the ratios decrease with height, it implies that the outflow speed increases. The effect is stronger for the CH region. At small heights, the ratio decreases with time which is likely due to the increase in the line-of-sight electron density as the active regions rotate toward the limb. At large heights, the ratio increases with time implying decreasing outflow speed and it seems to happen mainly at the first two days. This is consistent with the fast to slow wind transition in the ACE data. Note that on Oct. 18 at 3.5 and $4.5 R_{\odot}$, we need to combine the CT and CH data to get good statistics for OVI 1037, so the OVI ratio is the same for both regions.

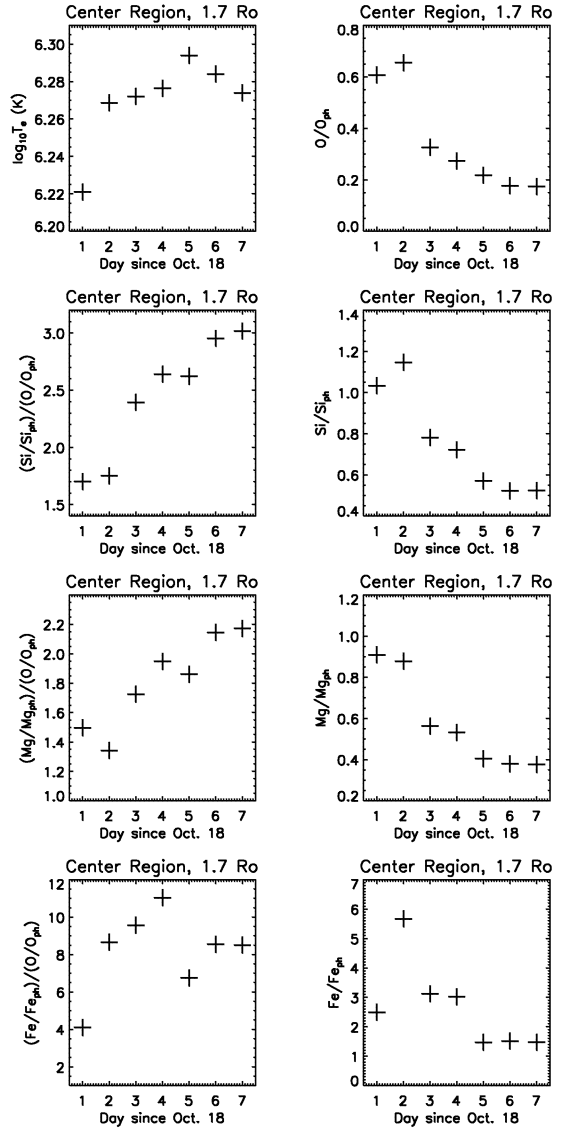


FIGURE 7. The electron temperature and elemental abundance from the CT region at $1.7 R_{\odot}$ plotted versus time.

At $1.7 R_{\odot}$, the abundance data allow us to obtain the electron temperature from the line ratios of Fe X 1028, [Fe XII] 1242, and Fe XIII] 510 assuming a single temperature along the line of sight. We can then obtain estimates for the elemental abundance from line ratios relative to O or H [9]. A more confident result is obtained in the CT region where these lines are brighter. Fig. 7 plots the resulting T_e and X/X_{ph} (absolute abundance which is relative to H, right panels in Fig.7) and $(X/X_{ph})/(O/O_{ph})$. They are from O: OVI 1032 abundance data, Si: the average of Si XII 520 abundance data and Si XII 499 intensity data; Mg: Mg X 609 intensity data; Fe: [Fe XII] 1242 abundance data. We can see that $(Si/Si_{ph})/(O/O_{ph})$ and $(Mg/Mg_{ph})/(O/O_{ph})$ increase with time, while $(Fe/Fe_{ph})/(O/O_{ph})$ does not have any systematic trend. Both T_e and the abundance relative to O seem to be consistent with the solar wind data (Fig.3). However, the systematic change of these parameters in the CT region has a time scale longer than that in the solar wind (~ 2 days). The absolute abundances all show a decrease with time. At this moment, we do not have an explanation for this phenomenon. The solar wind abundance data relative to hydrogen may help to shed some light on if this dependence is actually associated with the solar wind.

DISCUSSION

The line widths and OVI ratios in the CH region indicate that the line of sight is dominated by the coronal hole. On the other hand, the CT region is dominated by the hot and dense materials above the active region loops. Nevertheless, we find a likely correlation in T_e and elemental abundances in the CT region with the solar wind. This may have some implication on associating the origin of the slow wind with mixing of the closed field materials, although our analysis at this point is not conclusive.

Elemental abundance is thought to be a clear distinguisher for the fast and slow solar wind by their FIP effect. Our preliminary analysis here indicates that it is not straightforward to make these calculations for the corona. Elemental abundances in the corona are difficult to obtain due to the line-of-sight effects. Also the methods to determine the electron temperature and abundances are subject to various uncertainties [16]. Some ions (e.g. Si XII, Fe X) are more sensitive to the temperature in the temperature range of concern than the others (e.g. O VI, Mg X, Fe XII), thus a small uncertainty in T_e results in large uncertainty in the abundances derived

from some lines. A more complete and detailed analysis, incorporating other aspects of this data set with Doppler dimming modelling and the solar wind data (e.g. abundance to H, charge composition) will be presented in a future paper.

ACKNOWLEDGMENTS

This work is supported by NASA grant NAG5-10093. SOHO is a joint mission of ESA and NASA.

REFERENCES

1. Geiss, J., Gloeckler, G., and von Steiger, R., *Space Sci. Rev.*, **72**, 49-60 (1994).
2. Hundhausen, A. J., Gilbert, H. E., and Bame, S. J., *Astrophys. J.*, **152**, L3-L5 (1968).
3. Owocki, S. P., Holzer, T. E., and Hundhausen, A. J., *Astrophys. J.*, **275**, 354-366 (1984).
4. Ko, Y.-K., G., Fisk, L., Geiss, J., Gloeckler, G., and Guhathakurta, M., *Solar Physics*, **171**, 345-361 (1997).
5. von Steiger, R., and Geiss, J., *Astron. Astrophys.*, **225**, 222-238 (1989).
6. Peter, H., and Marsch, E., *Astron. Astrophys.*, **333**, 1069-1081 (1998).
7. Kohl, J. L. et al., *Solar Phys.*, **162**, 313-356 (1995).
8. Kohl, J. L., et al., *Solar Phys.*, **175**, 613-644 (1997).
9. Raymond, J. C. et al., *Solar Phys.*, **175**, 645-665 (1997).
10. Gloeckler, G. et al., *Space Sci. Rev.*, **86**, 495 (1998).
11. Linker, J. A. et al., *J. Geophys. Res.*, **104**, 9809-9830 (1999).
12. Riley, P., Linker, J. A., and Mikic, Z., 'Solar cycle variations and the structure of the heliosphere: MHD simulations', submitted to Proceedings of Chapman Conference on Space Weather, April 2000.
13. Mikic, Z., Linker, J. A., Schnack, D. D., Lionello, R., and Tarditi, A., *Phys. Plasmas*, **6**, 2217 (1999).
14. Noci, G., Kohl, J. L., and Withbroe, G. L., *Astrophys. J.*, **315**, 706-715 (1987).
15. Cranmer, S. R., Field, G. B., and Kohl, J. L., *Astrophys. J.*, **518**, 937-947 (1999).
16. Raymond, J. C. et al., this volume (2001).